2014 ASIA-PACIFIC SOLAR RESEARCH CONFERENCE

# An Integrated Optical and Thermal Model of Cavity Receivers for Paraboloidal Dish Concentrators

Jose I. Zapata[1], Charles-Alexis Asselineau[1], John Pye[1], Martin Kaufer[3] and Graham Hughes[2]
[1]*Research School of Engineering, ANU, Bldg 32 North Rd, Canberra, Australia*
[2]*Research School of Earth Sciences, ANU, Bldg 142 Mills Rd, Canberra, Australia*
*E-mail: jose.zapata@anu.edu.au*

**Abstract**
This paper presents an integrated numerical model of the heat transfer in axi-symmetrical cavity receivers powered by a paraboloidal dish concentrator. Receivers under consideration are once-through to superheated steam boilers consisting of a single path of helical tubing. The integrated model calculates the thermal performance of a receiver in steady state, combining ray tracing, hydrodynamic and CFD simulations. The model provides a design tool for an ongoing effort at the ANU to optimise the performance of a receiver by adjusting the design of the cavity shape and tube profile. This paper describes the integrated model with an emphasis on the hydrodynamic receiver model, as it is in this instance where the conservation equations for the receiver model are solved. Key outputs from the model include flux distribution within the cavity, fluid, inner- and outer-wall temperature distributions, local heat transfer coefficient, pressure drop, and a breakdown of the losses by different heat transfer mechanisms. The paper concludes with representative results for two prospective receiver designs, as an example of the process being used for an ongoing optimisation of receiver cavity geometries for dish systems.

## 1. Introduction

In a conventional concentrating solar-thermal power (CSP) plant, the receiver absorbs concentrated solar radiation and transfers it to a medium. The medium in turn transports the heat to thermal energy storage and eventually to a power cycle for generation of electricity. With high-concentration solar flux on its outward-facing surfaces, receivers can have significant levels of convective and radiative heat loss, which must be minimised in order for the resulting electricity to be cost-competitive with alternative energy sources (Bannister, 1991, Ho, 2014, Taumoefolau et al., 2004).

As a part of a project to design improved receivers with reduced thermal losses, this paper presents an integrated model to simulate the behaviour of a variety of axi-symmetric cavity receiver designs for a paraboloidal dish concentrator (Lovegrove et al., 2011). This numerical model tool arises from the need to characterise the steady state behaviour of receivers of different shapes, and thus to distinguish which aspects of the cavity geometry design improve the thermal performance of such receivers.

All geometries under consideration are composed of a helically-coiled tube that winds from the outer edge of the receiver aperture to the central rear inside the cavity. The tube can feature a variety of wall thicknesses and diameters, even within a single geometry. The model integrates all the significant heat transfer processes occurring in the receiver: incident solar flux distribution on the tube; blockage, spillage and reflection losses; thermal emission losses; thermal resistance through receiver tubes and surface coatings; and internal flow boiling heat transfer. Pressure drops in the internal flow due to friction are also considered.

The paper first describes the type of receiver cavity geometries under consideration, followed by a description of the integrated modelling approach. Then the paper describes the incorporation of interaction ray tracing and CFD data, and it concludes preliminary results that will form the basis for a cavity receiver design at the ANU.

## 2. Receiver cavity geometries

The integrated model in this study evaluates the thermal performance of multiple receiver geometries, as part of a larger study to design optimised receivers for parabolic dish systems. The receiver geometries under consideration are axially symmetric along the depth axis of the cavity. To cover a wide range of cases, receiver geometries in this study are defined as an arbitrary number of truncated conical sections, each with variable dimensions. Figure 1 shows a diagram of an example cavity composed of 3 conical sections.

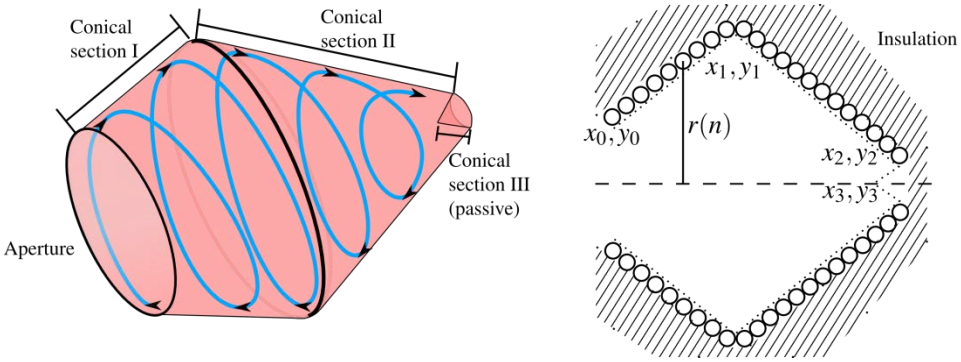


**Figure 1 (Left) Basic receiver geometry composed of three conical sections. (Right) Cavity receiver cross section, showing absorber tube loops.**

All geometries considered in this study are modelled as once-through to superheated steam receivers. These receivers consist of a single path of helical tube circumscribing the basic receiver shape (see Figure 1 right). Water traverses the helical receiver tube path, starting at the aperture and exiting at the back of the cavity. Tube materials available for selection are subject to minimum bending radius constraints, so all basic geometries under consideration include a small conical section at the back of the cavity with no tubes, termed a passive section. Concentrated radiation from the parabolic dish enters through the cavity aperture and hits the cavity side of the tubes, and the passive section. Operating mass flows considered in this study are such that water turns into super-heated steam at a set temperature in a single pass. The temperature profile in the receiver tube results from the interaction between incident radiation on the tubes, heat absorbed by the water (in single and two-phase flow) and thermal losses through the receiver.

## 3. Integrated model of heat transfer in the receiver geometry

The integrated model simulates the thermal performance of receiver geometries in steady state operation with the receiver as mounted at the focus of a parabolic dish tracking the sun, and a mass flow that results in a set steam temperature at the receiver outlet. In order to assemble this simulation, the integrated model has to combine three separate simulation domains, and combine their results in a common geometry definition for the receiver.

### *3.1. Integration across 3 simulation domains*

To reach a solution, the integrated model must combine the results from three simulation domains: Ray tracing, hydrodynamic and Computational Fluid Dynamic (CFD). Ray tracing simulations solve all the optical aspects of the scene: incident solar radiation, blockage and spillage losses caused by the receiver geometry, reflection and focusing on the dish concentrator, reflection off the tube surface and heat absorbed by the receiver tubes (Asselineau, Abbasi & Pye, 2014, Asselineau, Zapata & Pye, 2014). Hydrodynamic simulations solve the boiling profile in the receiver tube, by accounting for energy gain and phase change in the fluid for the given amount of absorbed radiation. CFD simulations calculate natural convection losses in the cavity, for a given internal surface profile.

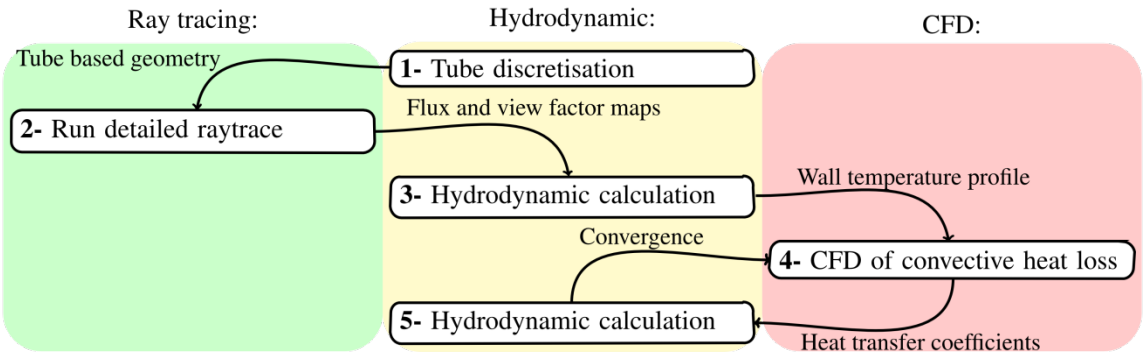


**Figure 2 Integrated model calculation stages across three simulation domains**

Figure 2 shows a diagram of the calculation stages if the integrated model. Simulations exchange data to combine different heat transfer mechanisms in a single cavity geometry solution. The integrated model defines a common interface between simulation domains that matches the discretisation of the receiver tube in the cavity geometry. With this approach, the integrated model can evaluate a local energy balance for a portion of the tube that couples radiative, natural and forced convection heat transfer.

### *3.2. Receiver tube discretization*

Due to the spatially distributed nature of all heat transfer mechanisms in the integrated model, this study divides the receiver tube into discrete segments along its length, and solves the energy balance in the receiver with a finite difference approach. The distribution of incoming radiation in a given cavity geometry is radially symmetric, but varying along the depth axis of the cavity. This is because both the receiver cavity geometries and the paraboloidal dish concentrator are assumed radially symmetric in ray tracing simulations. Therefore, the receiver tube is divided into segments spanning approximately one `loop' around the helical path of the tube in the cavity (see Figure 1). For each of the resulting tube segments, incoming concentrated radiation is approximately uniform.

For a given tube diameter, the actual path described along that section will seldom result in an integer number of loops. To produce axially symmetric segments, the integrated model needs to produce an integer number of loops in a conical section. The integrated model first calculates the total length of the helically coiled path along a conical section. Then, the model slices the conical section into depth sections equal to the number of complete loops of tube. These conical section slices/segments will be slightly wider than the outside tube diameter specified for the conical section. The integrated model redistributes the length of the remaining 'partial' tube loop evenly onto the length of the complete loops segments, to compensate for this disparity.

## 4. Hydrodynamic model of the receiver tube

The hydrodynamic model determines the temperature profile in the absorber tube when balancing incoming radiation, optical/thermal losses and the heat absorbed by the fluid passing through the receiver. The tube wall temperature profile is crucial to obtain a solution for a given receiver geometry, and is thus at the core of the integrated receiver model

### *4.1. Conservation of energy in the tube wall*

The hydrodynamic model in this study establishes a finite-difference thermal energy balance in the receiver tube wall. The balance is derived from first principles of mass, energy and momentum conservation, and accounts for the heat exchanged on the inside and outside of the

tube. Figure 3 shows a diagram of the energy balance in a single segment in the model (see nomenclature).

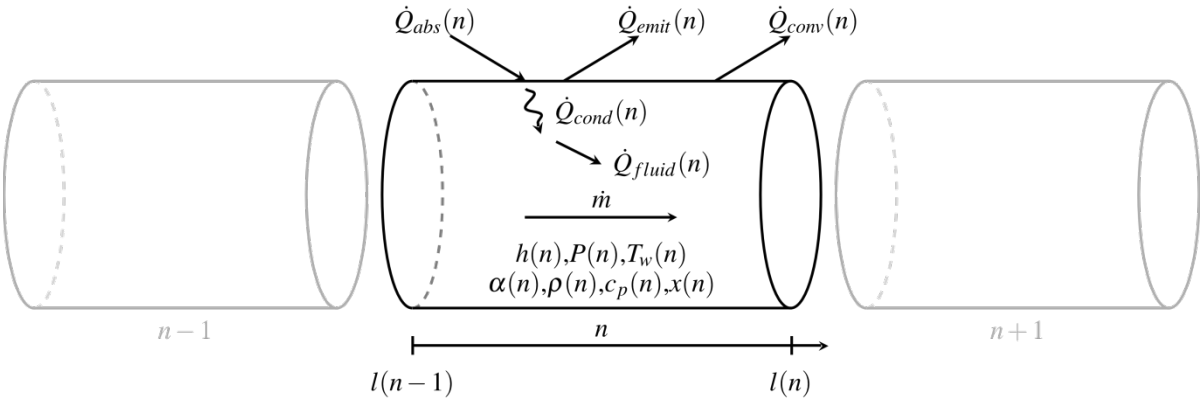


**Figure 3 Energy balance diagram for a tube segment *n* in the receiver geometry**

For each receiver tube segment $n$, the energy balance considers: the heat absorbed by the fluid through forced convection $\dot{Q}_{fluid}(n)$, the heat conducted through the tube wall $\dot{Q}_{cond}(n)$, the convective heat loss from the tube wall into the air in the cavity $\dot{Q}_{conv}(n)$, the grey body diffuse radiation emitted by the segment into the cavity $\dot{Q}_{emit}(n)$, and the concentrated radiation absorbed by the tube $\dot{Q}_{abs}(n)$, after discounting reflection off the tube surface. The hydrodynamic model assumes a constant mass flow $\dot{m}$ through all segments in the tube.

All heat transfer mechanisms in the wall tube energy balance (except for $\dot{Q}_{abs}(n)$) affect each other in function of outside wall temperature $T_{wo}(n)$. The hydrodynamic simulation varies $T_{wo}(n)$ to reach a solution that conserves all energy terms in the system.

$$\dot{Q}_{abs}(n, T_{wo}(n)) = \dot{Q}_{emit}(n, T_{wo}(n)) + \dot{Q}_{conv}(n, T_{wo}(n)) + \dot{Q}_{cond}(n, T_{wo}(n)) \quad (1)$$

From the tube outer wall temperature and mass flow, the model needs to also determine the heat absorbed by the fluid.

### *4.2. Conduction through the tube wall*

The model considers an inner tube wall temperature $T_{wi}(n)$ and an outer tube wall temperature $T_{wo}(n)$. The gradient between these two temperatures depends on the heat conduction through the heated side of the tube.

$$\dot{Q}_{cond}(n) = \frac{\pi l(n)(T_{wo}(n) - T_{wi}(n))}{\ln\frac{D_o(n)}{D_i(n)}/k + \ln\frac{D_o(n) + d_c(n)}{D_o(n)}/k_c} \quad (2)$$

This calculation incorporates the thickness of the tube segment and its conductivity. It can also include a coating with a thickness $d_c(n)$ and conductivity $k_c(n)$.

### *4.3. Forced heat transfer convection into the fluid*

The model can determine all fluid properties in the segment from bulk fluid enthalpy, $h_f(n)$ bulk fluid pressure $P_f(n)$ and steam table correlations (Wagner & Pruss, 2002). The hydrodynamic model solves a localised energy balance in each segment as a finite difference to compute the enthalpy gain for the fluid:

$$h_o(n) = h_i(n) + \frac{\pi D_i(n) l(n)}{2} \frac{\alpha(n)\left(T_{wi}(n) - T_f(n)\right)}{\dot{m}} \quad (3)$$

The forced convection heat transfer $\alpha(n)$ is calculated from correlations of single and two-phase flow of water, at bulk fluid properties. If the fluid is single phase (i.e. liquid water or super-heated steam), $\alpha(n)$ is calculated using correlations by Gnielinski (Gnielinski, 1976) for $Re < 10^5$ and Petukhov and Popov (Petukhov & Popov, 1963) for $Re \geq 10^5$. If the fluid is a saturated water-vapour mixture with a steam quality in the range $0 < x < 0.8$, the model employs a correlation by Kandlikar (Kandlikar, 1991). For steam qualities in the range $0.8 \leq x < 1$ the hydrodynamic model employs a post dry-out correlation by Groenveld (Groeneveld, 1973).

A simplified momentum balance in the pipe segment accounts for pressure drop:

$$P_o(n) = P_i(n) - \frac{\dot{m}^2 f(n) l(n)}{2\rho A^2 D_i(n)} \tag{4}$$

Friction factor calculations and consequently convection heat transfer coefficients include a multiplier to account for coiling effects in the tube (Mishra & Gupta, 1979).

### *4.4. Natural convection heat loss*

The amount of heat lost by a tube segment to the cavity due to natural convection is:

$$\dot{Q}_{cond}(n) = U(n) D_o(n) l(n) (T_{wo}(n) - T_{wi}(n)) \tag{5}$$

The transfer coefficient $U(n)$ is obtained iteratively from CFD simulations. First, a hydrodynamic simulation of the receiver with no convective losses generates a temperature profile of the receiver surface, and this profile becomes a boundary condition for CFD simulations. CFD simulations then produce a net heat flux for the segment from natural convection, from which $U(n)$ is derived. This heat transfer coefficient alters the temperature distribution in the cavity, so the procedure has to be repeated a second time to achieve convergence (i.e. steps 4 and 5 in Figure 2).

### *4.5. Grey body radiative emissions and absorbed radiation*

The amount of radiative heat emitted by each segment in the cavity is obtained with the radiosity method. For each segment, the resulting heat emission is thus:

$$\dot{Q}_{emit}(n) = D_o(n) l(n) \frac{\varepsilon(n)}{1 - \varepsilon(n)} (\sigma T_{wo}^4(n) - J(n)) \tag{6}$$

$J(n)$ is the radiant flux in the infra-red spectrum captured by the tube segment from all other surfaces in the cavity. The view factors between all the segments in the cavity plus the passive section are pre-calculated in ray tracing simulations and saved as a data file. The hydrodynamic simulation accesses this data file and solves the radiosity equations by matrix inversion every time the tube surface temperatures change.

### *4.6. Simulation procedure*

Figure 4 shows a diagram with the solution procedure for the hydrodynamic model. The solution requires three nested iteration loops to ensure the convergence of all calculations. The calculation requires a ray tracing simulation of the cavity before starting, and it can only interface with CFD simulations after ending. The role of the outermost loop is to seek an outlet temperature $T_{o=}500$ °C[1] by adjusting the mass flow $\dot{m}$. Each time a new mass flow is set, the two inner loops must be repeated to ensure a reliable calculation of the boiling profile.

[1] Or another arbitrarily set outlet temperature

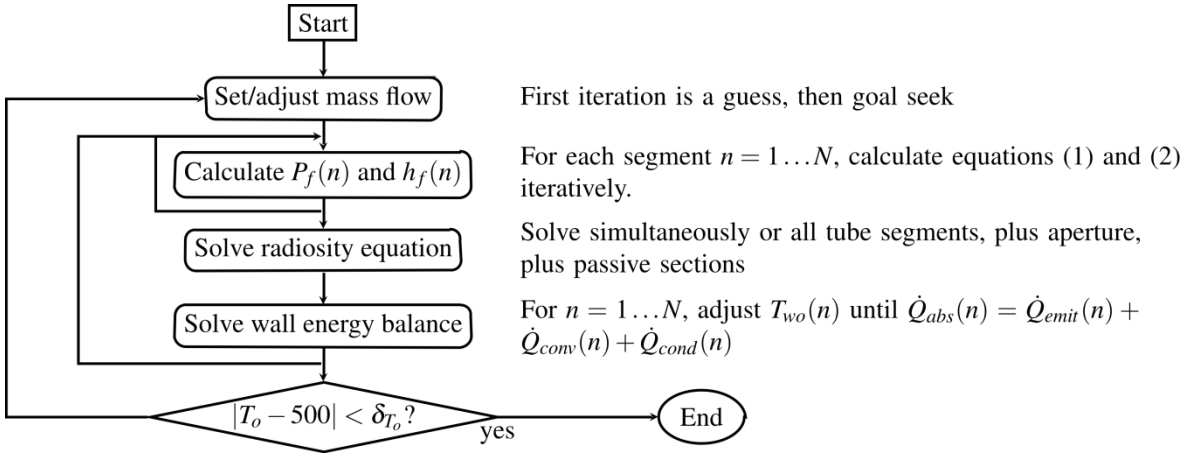


**Figure 4 Solution procedure for the hydrodynamic model of the receiver tube**

## 5. Simulated boiling profiles

Figure 5 shows integrated receiver model simulation results for two sample receiver geometries. All simulations consider a paraboloidal dish of 489 m$^2$ of aperture, 90% average reflectivity and focal length of 13.4 m. Additional conditions include DNI=1000 W/m$^2$, outlet temperature $T_o = 500$ ℃, ambient temperature $T_a = 25$ ℃, an inclination angle of 30° and an insulation cladding of 100mm thick mineral wool surrounding the outside of the cavity.

The top panels show a cross section of two candidate receiver geometries overlaid with the absorbed heat flux distribution (grey colour map) and with the outside wall tube distribution (orange colour map). The stacked graph at the right of each diagram is the breakdown of heat losses in kW. The integrated model reveals how the dimensions of each receiver significantly affect the distribution of concentrated radiation on the cavity surface.

For the receiver on the right, the peak heat flux occurs approximately in the middle of the geometry and it is roughly aligned with the portion of tube occupied by saturated two-phase flow. The receiver on the left is subject to the most intense flux at the back of the cavity, where the fluid is superheated steam.

Below each receiver diagram is the corresponding tube boiling profile for the geometry. Tube boiling profiles show outside and inside tube wall temperatures as well as the temperature of the fluid. Vertical dotted lines demarcate the boundary between conical sections in the geometry with respect to tube length. These profiles show that the dominant phenomena shaping the wall temperature distribution on the tubes is how the fluid evolves as it passes through the receiver and the distribution of heat flux in the cavity. The cavity on the left has intense flux near the narrowest point near the aperture, and this drives an early onset of saturated two-phase flow. Conversely, the cavity on the right has less intense flux, and exhibits a more gradual boiling profile. The cavity on the right has more intense flux at the back of the cavity, creating a large temperature difference between the tube wall and the fluid near the ‘dry-out’ region of two-phase flow. This situation poses a challenge to the selection of tube materials, because under these conditions, the tube would be under significant thermal stress.

The bottom panels show the pressure drop profile and the calculated internal heat transfer coefficient for the fluid below the boiling profiles for both cavities. The integrated model finite element enables the calculation of local fluid properties, which in turn results in more accurate heat transfer calculations for all the mechanisms involved in the receiver.

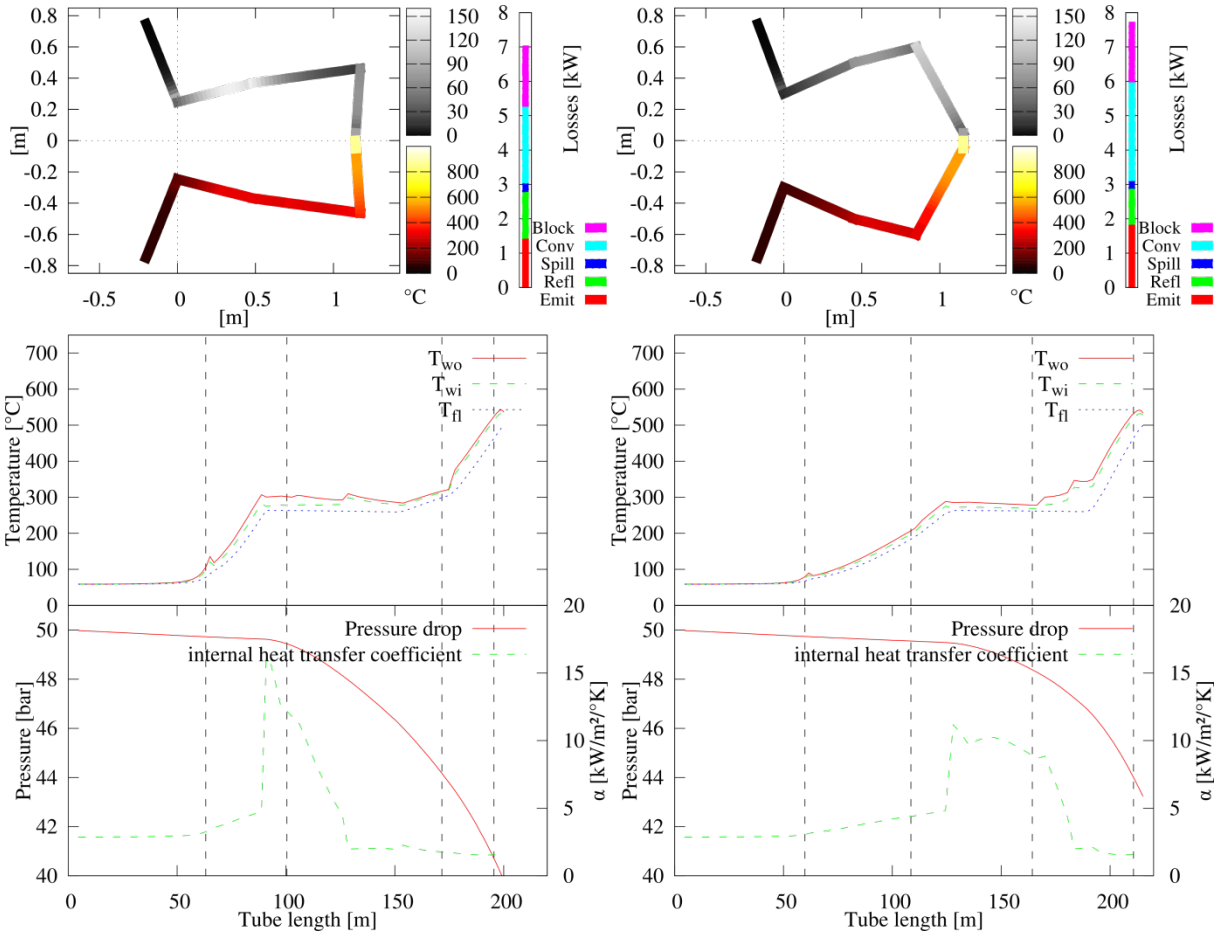


**Figure 5 Simulation Results for two sample geometries.**

## 6. Summary

This paper described an integrated numerical heat transfer model of axi-symmetric cavity receivers. The integrated model can handle a variety of receiver geometries by parameterising the cavity as a series of conical sections. This basic geometry defines the envelope for a single path of helical tube that becomes the actual receiver cavity. The model segments the receiver tube into `loops' to solve the energy balance in the receiver with a finite-difference method. All cavity geometries are simulated as once-through to superheat receivers powered by a parabolidal dish. The integrated model combines ray tracing, hydrodynamic and CFD simulation results to couple radiative, convective, natural and forced convection heat transfer phenomena in the receiver. The resulting simulations provide a detailed account of the temperature profile of the receiver tube and the fluid passing through it. With these profiles, it is possible to estimate the thermal performance of any given receiver cavity geometry, and thus explore new receiver designs that offer higher thermal efficiencies when operating with parabolidal dish concentrators.

## References

Asselineau, C.-A., Abbasi, E. & Pye, J. (2014), Open cavity receiver geometry influence on radiative losses, *in* 'Solar2014: The 52nd Annual Conference of the Australian Solar Council'.

Asselineau, C.-A., Zapata, J. & Pye, J. (2014), 'Geometrical shape optimisation of a cavity receiver using coupled radiative and hydrodynamic modelling', *Energy Procedia* -, –. under review.

Bannister, P. (1991), 'Maximisation of exergy gain in high temperature solar thermal receiver by choice of pipe radius', *Journal of Heat Trans* **113**, 337–340.

Gnielinski, V. (1976), 'New equations for heat and mass transfer in turbulent pipe and channel flow', *Int. Chem. Eng* **16**(2), 359–368.

Groeneveld, D. (1973), Post-dryout heat transfer at reactor operating conditions, Technical report, Atomic Energy of Canada Ltd., Chalk River, Ontario. Chalk River Nuclear Labs.

Ho, C. K. (2014), 'Computational fluid dynamics for concentrating solar power systems', *Wiley Interdisciplinary Reviews: Energy and Environment* **3**(3), 290–300. http://dx.doi.org/10.1002/wene.90

Kandlikar, S. G. (1991), 'Development of a flow boiling map for subcooled and saturated flow boiling for different fluids inside circular tunes', *Journal of Heat Transfer* **113**, 191–200.

Lovegrove, K., Burgess, G. & Pye, J. (2011), 'A new 500 m2 paraboloidal dish solar concentrator', *Solar Energy* **85**(4), 620 – 626. http://www.sciencedirect.com/science/article/B6V50-4YDX8S1-1/2/6d8cfa1345e4ca4ffa2f6ba7472eb4ed

Mishra, P. & Gupta, S. (1979), 'Momentum transfer in curved pipes. 1. newtonian fluids', *Ind. Eng. Chem. Process Des. Dev.* **18**(1), 130–137.

Petukhov, B. & Popov, V. (1963), 'Theoretical calculation of heat exchange and frictional resistance in turbulent flow in tubes of an incompressible fluid with variable physical properties(heat exchange and frictional resistance in turbulent flow of liquids with variable physical properties through tubes)', *High Temperature* **1**, 69–83.

Taumoefolau, T., Paitoonsurikarn, S., Hughes, G. & Lovegrove, K. (2004), 'Experimental investigation of natural convection heat loss from a model solar concentrator cavity receiver', *J. Sol. Energy Eng.* **126**(2), 801–807.

Wagner, W. & Pruss, A. (2002), 'The IAPWS formulation 1995 for the thermodynamic properties of ordinary water substance for general and scientific use', *Journal of Physical and Chemical Reference Data* **31**(2), 387–535.

| | |
|---|---|
| $n$ | Index denoting a single pipe segment in simulations |
| $P_i(n)$ | Pressure at segment inlet in bar |
| $P_o(n)$ | Pressure at element outlet in bar |
| $P_f(n)$ | Bulk pressure in segment $P_f(n) = P_i(n)/2 + P_o(n)/2$ in bar |
| $h_i(n)$ | Fluid enthalpy at segment inlet in kJ kg$^{-1}$ |
| $h_o(n)$ | Fluid enthalpy at segment outlet in kJ kg$^{-1}$ |
| $h_f(n)$ | segment bulk enthalpy $h_f(n) = h_i(n)/2 + h_o(n)/2$ kJ kg$^{-1}$ |
| $T_{wi}(n)$ | Tube inner wall temperature in °C |
| $T_{wo}(n)$ | Tube outer wall temperature in °C |
| $T_f(n)$ | segment bulk fluid temperature $T_f(n) = \Phi_f(P_f, h_f)$ |
| $T_a$ | Ambient temperature in °C |
| $D_i(n)$ | Tube inner diameter in m |
| $D_o(n)$ | Tube outer diameter in m |
| $l(n)$ | Segment tube length |
| $f(n)$ | Friction factor |
| $\alpha(n)$ | Segment fluid forced convection heat transfer coefficient in kW m$^{-2}$ |
| $\dot{Q}_{emit}$ | Segment thermal emission. In kW. |
| $U(n)$ | segment natural convection coefficient to air (cavity side, calculated by CFD) in kW m$^{-2}$ |
| $\dot{Q}_{abs}(n)$ | segment absorbed concentrated radiation. In kW (calculated by Raytracing) |
| $A(n)$ | segment surface area, used in ray tracing and view factor calculations. In m$^2$ |
| $\varepsilon(n)$ | Tube emissivity |
| $a(n)$ | Tube absorptivity |
| $k(n)$ | Tube conductivity |
| $k_c(n)$ | Tube coating conductivity |
| $\dot{m}$ | Mass flow along the tube in kg s$^{-1}$ |

## Acknowledgements

The authors would like to acknowledge the wealth of insightful comments provided by Joe Coventry, Felix Venn, Greg Burges and Ehsan Abbasi. This research was performed as part of the Australian Solar Thermal Research Initiative (ASTRI), a project supported by the Australian Government, through the Australian Renewable Energy Agency (ARENA). Responsibility for the views, information or advise expressed herein is not accepted by the Australian Government.